AGU PUBLICATIONS

Geochemistry, Geophysics, Geosystems

RESEARCH ARTICLE
10.1002/2016GC006735

Key Points:
- Iron and zinc stable isotope and elemental data are presented for a prograde suite of metabasalts and metagabbros from Western Alpine ophiolite complexes
- Bulk rock δ^{56}Fe and δ^{66}Zn do not vary across metamorphic facies and the eclogitic samples show a MORB-like isotope composition
- Blueschist facies metagabbros preserve evidence for infiltration of sediment derived fluids that impart a light δ^{56}Fe isotope composition to the gabbro

Supporting Information:
- Supporting Information S1
- Table S1
- Table S2

Correspondence to:
E. C. Inglis,
e.c.inglis@durham.ac.uk

Citation:
Inglis, E. C., et al. (2017), The behavior of iron and zinc stable isotopes accompanying the subduction of mafic oceanic crust: A case study from Western Alpine ophiolites, *Geochem. Geophys. Geosyst.*, *18*, 2562–2579, doi:10.1002/2016GC006735.

Received 16 NOV 2016
Accepted 2 JUN 2017
Accepted article online 9 JUN 2017
Published online 13 JUL 2017

The behavior of iron and zinc stable isotopes accompanying the subduction of mafic oceanic crust: A case study from Western Alpine ophiolites

Edward C. Inglis[1], Baptiste Debret[1,2], Kevin W. Burton[1], Marc-Alban Millet[1,3], Marie-Laure Pons[1,2], Christopher W. Dale[1], Pierre Bouilhol[1,4], Matthew Cooper[5], Geoff M. Nowell[1], Alex J. McCoy-West[1], and Helen M. Williams[1,2]

[1]Department of Earth Sciences, Science Labs, Durham University, Durham, UK, [2]Department of Earth Sciences, University of Cambridge, Cambridge, UK, [3]School of Earth and Ocean Science, Cardiff University, Cardiff, UK, [4]Université Clermont Auvergne, CNRS, IRD, OPGC, Laboratoire Magmas et Volcans, Clermont-Ferrand, France, [5]Ocean and Earth Science, National Oceanography Centre Southampton, University of Southampton, Southampton, UK

Abstract Arc lavas display elevated $Fe^{3+}/\Sigma Fe$ ratios relative to MORB. One mechanism to explain this is the mobilization and transfer of oxidized or oxidizing components from the subducting slab to the mantle wedge. Here we use iron and zinc isotopes, which are fractionated upon complexation by sulfide, chloride, and carbonate ligands, to remark on the chemistry and oxidation state of fluids released during prograde metamorphism of subducted oceanic crust. We present data for metagabbros and metabasalts from the Chenaillet massif, Queyras complex, and the Zermatt-Saas ophiolite (Western European Alps), which have been metamorphosed at typical subduction zone *P-T* conditions and preserve their prograde metamorphic history. There is no systematic, detectable fractionation of either Fe or Zn isotopes across metamorphic facies, rather the isotope composition of the eclogites overlaps with published data for MORB. The lack of resolvable Fe isotope fractionation with increasing prograde metamorphism likely reflects the mass balance of the system, and in this scenario Fe mobility is not traceable with Fe isotopes. Given that Zn isotopes are fractionated by S-bearing and C-bearing fluids, this suggests that relatively small amounts of Zn are mobilized from the mafic lithologies in within these types of dehydration fluids. Conversely, metagabbros from the Queyras that are in proximity to metasediments display a significant Fe isotope fractionation. The covariation of δ^{56}Fe of these samples with selected fluid mobile elements suggests the infiltration of sediment derived fluids with an isotopically light signature during subduction.

1. Introduction

Oceanic lithosphere formed at mid-ocean ridges is progressively hydrated, altered, and oxidized by interaction with seawater before being recycled into the deep mantle at convergent plate margins. During the subduction of oceanic lithosphere, the increase in pressure and temperature (*P-T*) conditions leads to the destabilization of hydrous mineral phases via a series of metamorphic reactions and the release of dehydration fluids and/or slab derived melts into the overlying crust and subarc mantle [e.g., *Schmidt and Poli*, 2014; *Hermann and Green*, 2001; *Bouilhol et al*., 2015]. Alongside the release of structurally bound H_2O from subducted sediments, mafic and ultramafic sections of the slab, the mechanical compaction of sediments at shallower depths (<20 km) can result in pore fluid expulsion in the fore arc region [*Hensen et al*., 2004; *Rüpke et al*., 2004] and localized metasomatism of lithologies in the residual subducting slab [e.g., *Marschall et al*., 2009; *Penniston-Dorland et al*., 2012; *Vitale Brovarone and Beyssac*, 2014; *Debret et al*., 2016a]. The release of slab derived subcritical [*Hermann et al*., 2006] or supercritical [*Kessel et al*., 2005] fluids, and melts [*Foley et al*., 2000] has been invoked to explain a number of distinct geochemical signatures observed in arc lavas relative to mid-ocean ridge (MORB) and Ocean Island Basalts (OIB), including the enrichment of fluid mobile elements [*Hawkesworth et al*., 1993] and their elevated $Fe^{3+}/\sum Fe$ ratios [*Brandon and Draper*, 1996; *Frost and Ballhaus*, 1998; *Parkinson and Arculus*, 1999; *Kelley and Cottrell*, 2009]. At the same time, residual oceanic crust is ultimately recycled back into the deep mantle, providing a source for the geochemical heterogeneity that is sampled by MORBs and OIBs. Consequently, developing a clear understanding of the processes that govern element mobility during subduction zone metamorphism and metasomatism is crucial

for elucidating both the controls on arc magmatism and the long-term chemical evolution of the mantle [*Magni et al*., 2014]. This study aims to examine the effect of subduction zone metamorphism and metasomatism on the redox budget of subducted mafic oceanic crust using the stable iron (Fe) and zinc (Zn) isotopes as tracers of elemental mobility, which are thought to be sensitive to complexation by aqueous sulfate (SO_X) and carbonate (CO_X) ligands [*Fujii et al*., 2011; *Hill et al*., 2010; *Black et al*., 2011].

Recent advances in mass spectrometric techniques have seen the emerging field of nontraditional stable isotope geochemistry applied to numerous scientific problems in both high-temperature and low-temperature natural settings. Theory predicts that equilibrium stable isotope fractionation decreases with increasing temperature ($1/T^2$) [*Urey*, 1947; *Schauble*, 2004]. Nonetheless, high-precision Fe and Zn stable isotope measurements have shown that both of these systems are sensitive to high-temperature petrogenetic processes, such as mantle melting [*Weyer et al*., 2005; *Williams et al*., 2004, 2005, 2009; *Williams and Bizimis*, 2014; *Weyer and Ionov*, 2007; *Dauphas et al*., 2014; *Konter et al*., 2016], igneous differentiation [*Telus et al*., 2012; *Chen et al*., 2013; *Schuessler et al*., 2009; *Teng et al*., 2011, 2013; *Doucet et al*., 2016] and for Fe, changes in redox state [*Williams et al*., 2004; *Dauphas et al*., 2009]. It is now well established from both radiogenic and stable isotopes that the loss of fluid mobile elements from sediments imparts a distinct signature to arc lavas [e.g., *Pearce*, 1982; *Plank and Langmuir*, 1993; *Elliott et al*., 1997; *Nebel et al*., 2010; *Freymuth et al*., 2015], and the dissolution of carbonate sediments during subduction may play a role in controlling the redox budget of the subarc mantle [*Frezzotti et al*., 2011; *Evans*, 2012]. Despite this, it has been suggested that subducted sediments exert little influence on the Fe isotope composition of arc lavas, and that Fe isotope variations in erupted arc products result from depletion of the mantle source and fractional crystallization of the resulting melt [*Nebel et al*., 2015]. Additionally, the release of sulfur from the subducting slab could serve as a powerful oxidizing agent in this setting, as if sulfur was to be released from the slab as sulfate, then 1 mol of sulfur could serve to oxidize 8 mol of reduced Fe^{2+} to oxidized Fe^{3+}.

More recently, both Fe and Zn stable isotopes have been utilized to trace the mobility of Fe and oxidizing sulfate (SO_X) and/or carbonate (CO_X) species during the prograde devolitization of subducted slab serpentinites [*Debret et al*., 2016b; *Pons et al*., 2016]. However, while element depletion has been shown to occur from some parts of the mafic oceanic crust [e.g., *Dale et al*., 2007], the nature of those fluids remains poorly constrained. This study aims to examine the effect of subduction zone metamorphism on redox sensitive elements in mafic oceanic crust. To this end, we have measured stable Fe and Zn isotope in the metamorphic rocks of an exhumed subducted slab to trace the mobility of redox sensitive Fe and oxidizing SO_x/CO_x-rich fluids during the subduction-related, prograde metamorphism and metasomatism of the mafic oceanic crust.

One approach to assessing the controls on Fe and Zn isotopes during subduction-related metamorphism is to compare their behavior in oceanic crustal rocks across a range of *P-T* conditions. This study uses samples of metabasalts and metagabbros from three meta-ophiolite massifs in the Western European Alps—Chenaillet, Queyras, and Zermatt-Saas. These meta-ophiolites record prograde metamorphic conditions that range from greenschist to blueschist to eclogite that are taken to be representative of a *P-T* path for subducting mafic oceanic crust [e.g., *Guillot et al*., 2009] (Figure 1a). Samples have also been selected based on varying degree of fluid related slab metasomatism (i.e., those that show evidence for interaction with externally derived fluids released from proximal subducting sediments), thus allowing us to not only examine the effect of prograde metamorphism but also how metasomatic modification could potentially alter the Fe and Zn isotope composition of downgoing mafic lithologies.

2. Geological Setting and Sample Petrology

The ophiolite complexes of the Western European Alps provide a unique insight into the processes acting upon oceanic lithosphere during subduction [e.g., *Scambelluri and Philippot*, 2001; *Guillot et al*., 2009; *Debret et al*., 2013; *Vils et al*., 2011; *Evans et al*., 1979; *Hermann et al*., 2000; *Scambelluri et al*., 2001, 2014]. These meta-ophiolites were formed in a magma-poor setting, i.e., a slow or ultra-slow-spreading center or an ocean-continent transition, during the opening of the Ligurian Ocean in the Jurassic [*Lagabrielle and Cannat*, 1990; *Bernoulli et al*., 2003; *Lagabrielle et al*., 2015], before being subsequently metamorphosed at various *P-T* conditions and exhumed during the Alpine orogeny [*Rubatto et al*., 1998; *Brouwer et al*., 2004]. This study is focused on three Alpine ophiolitic complexes that record different *P-T* paths during Alpine

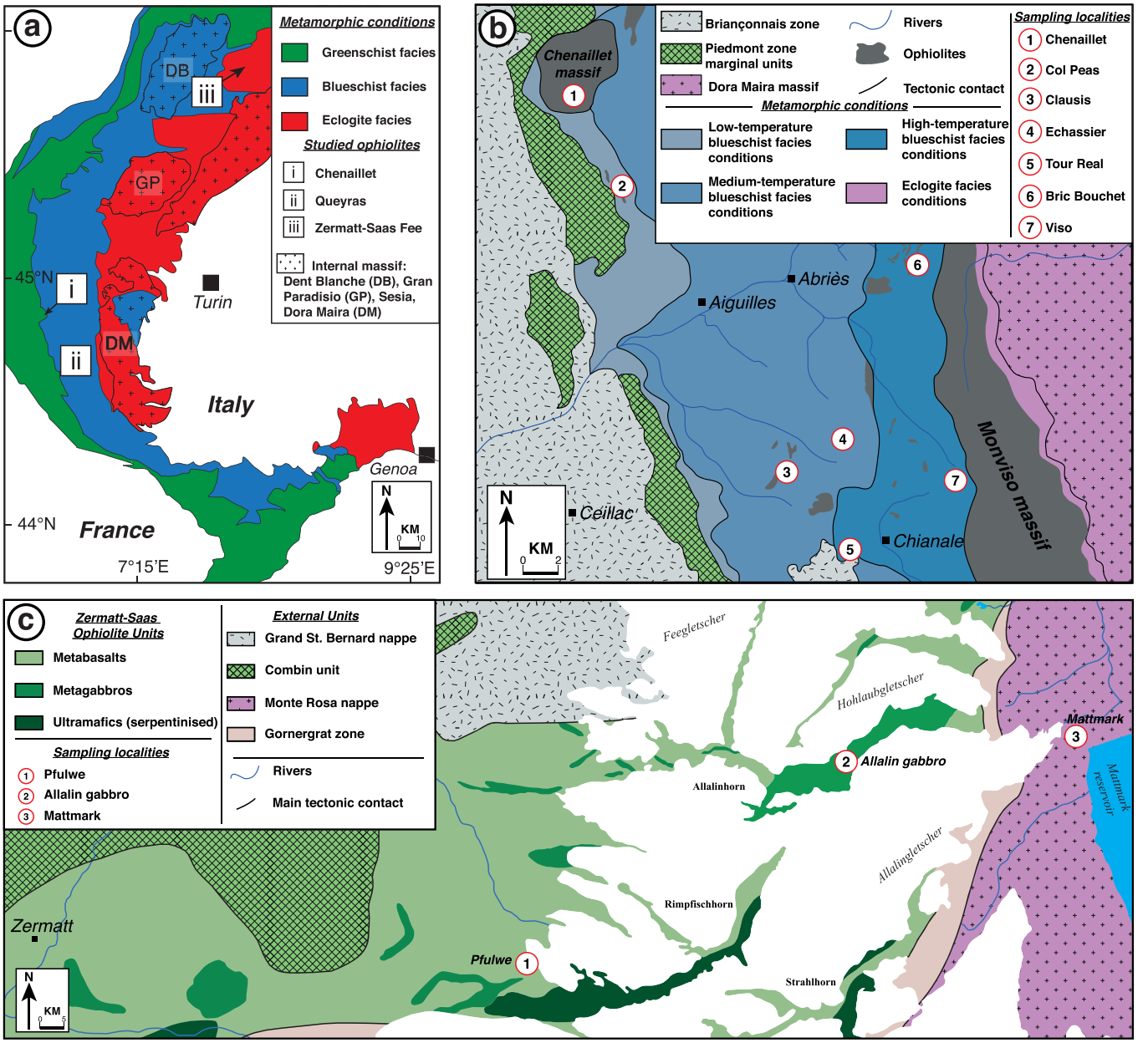

Figure 1. (a) The location of the three Western Alps ophiolitic complexes (Chenaillet, Queyras Schiste Lustrés, and Zermatt Saas) that were sampled as part of this study, within the context of Alpine metamorphic conditions. (b) The sampling localities for the Chenaillet massif and Queyras Schiste Lustré complex and the tectonometamorphic conditions within the area (modified after *Schwartz et al*. [2013]). (c) The sampling localities for the Zermatt-Saas area and the key lithological units of the complex.

evolution (Figure 1a). These are the Chenaillet massif, the Queyras Schiste-Lustrés, and Zermatt-Saas ophiolitic complexes. The Chenaillet massif mainly preserves low-pressure "ocean floor" parageneses, while the Queyras Schiste-Lustrés and Zermatt-Saas ophiolite complexes record the high-pressure transformation of subducted oceanic lithosphere, ranging from blueschist to eclogite facies, respectively.

2.1. The Chenaillet Massif

The Chenaillet massif is located in the external Piedmont zone, 6 km west of Briançon (Figure 1b). It is a structural klippe, overlying the Lago Nero-Replatte unit [*Caby*, 1995]. The massif preserves a classic sequence of oceanic lithosphere comprising, from top to bottom, oceanic sediments and/or basalts overlying gabbroic pods and serpentinized mantle peridotite. Detailed petrological, geochemical, and structural studies have suggested that this ophiolite represents a fossil oceanic core complex, likely formed at a slow-

spreading ridge setting [*Lagabrielle et al*., 1990; *Chalot-Prat*, 2005; *Manatschal et al*., 2011]. Unlike the majority of the Western Alpine ophiolites, the Chenaillet massif was only weakly affected by Alpine subduction [*Mevel et al*., 1978; *Debret et al*., 2016a]. Instead, the metagabbros here mainly record a low-pressure metamorphic overprint, ranging from amphibolite to greenschist facies conditions [*Mevel et al*., 1978; *Debret et al*., 2016a]. One coarse-grained metagabbro sample (PR4) was analyzed in this study. This sample represents an undeformed metagabbro, mainly composed of plagioclase and clinopyroxene. The clinopyroxene crystals display small ($\sim$20 μm) coronas of green and brown amphibole. Minor amounts ($<$10%) of actinolite are also observed, both within the plagioclase domain and associated with the amphibole coronas.

2.2. Queyras Schiste lustrés Complex

The Queyras Schiste lustrés complex is located in the Piedmont zone of the south-western Alps (Figure 1b). It comprises units belonging to the distal European margin and from the nearby oceanic domain [*Lemoine et al*., 1987] that were juxtaposed during Alpine subduction and collision in the Late Cretaceous to Tertiary [*Tricart*, 1984]. This complex comprises $\sim$10% meta-ophiolite bodies embedded in a sedimentary-rich environment, consisting of Jurassic to Lower Cretaceous clastic and metasedimentary rocks [*Lagabrielle et al*., 1984; *Lemoine et al*., 1987] and has previously been interpreted to represent a paleosedimentary wedge [*Tricart and Schwartz*, 2006].

Three tectonometamorphic domains have been identified within the complex by *Schwartz et al*. [2013]. The *P-T* conditions of these domains range from low-temperature blueschist facies conditions ($P = 0.9$–1.1 GPa, $T = 320$–340°C) in the west, to medium-temperature blueschist facies conditions ($P = 1.$–1.2 GPa, $T = 340$–360°C) and high-temperature blueschist facies conditions ($P = 1.2$–1.5 GPa, $T = 380$–470°C) toward the east (Figure 1b).

Eight metagabbros were collected from the medium-temperature and high-temperature blueschist domains within five different metagabbroic massifs. Four metagabbro samples were collected from the Echassier (CE7 and CE12) and Clausis (QE1 and QE10) meta-ophiolites that belong to the medium-temperature domain (Figure 1b). These samples predominantly display coarse-grained textures and are typically composed of clinopyroxene, partially recrystallized to glaucophane, while plagioclase is no longer present and is replaced by fine aggregate of lawsonite, chlorite and albite with minor amounts of ilmenite, titanite and late zoisite. Within these massifs the interface between metasedimentary lithologies and metagabbros is demarked by metasomatic contacts, which represent a zone of intense localized fluid circulation, which has occurred during subduction [*Debret et al*., 2016a]. In order to constrain the nature of the fluid circulating within these zones during subduction, we selected a sample from one metasomatic contact (CE8a) from the Echassier meta-ophiolite. This sample comprises glaucophane, chlorite, quartz, epidote, and titanite. Four samples from the high-temperature domain were collected from the Refuge du Viso (RV7), Tour Real (TR6 and TR9), and the Bric Bouchet (BB1) meta-ophiolites (Figure 1b). The sample RV7 preserves relicts of brown amphibole associated with green amphibole coronas and partially recrystallized into glaucophane, while the plagioclase domain is recrystallized to fine aggregates ($<$10 μm) of lawsonite, chlorite, quartz, and magnetite. Samples TR6 and TR9 consist of lawsonite, magnetite, chlorite, and glaucophane without any low-pressure relicts, while BB1 displays a similar coarse-grained texture as the Tour Real samples but is composed of stretched porphyroblasts of brown amphibole in association with needles of tremolite and actinolite. In this sample, the plagioclase domain is finely recrystallized to aggregates of cloudy plagioclase and zoisite.

In addition to the metagabbro samples, two sedimentary lithologies from the low-temperature and high-temperature domains were also collected. One sediment sample (CP1) was taken from the Col Peas area within the low-temperature blueschist domain, while the second sediment sample (RV5) comes from the Refuge du Viso within the high-temperature domain. These samples are proximal within tens of meters to the sampled metagabbros. Both of these samples are similar in mineralogy and are comprised of calcite, quartz aggregates, stringy magnetite, phengite, chlorite, and titanite, with both preserving a well-developed foliation.

2.3. Zermatt-Saas

The Zermatt-Saas complex of Alpine Switzerland (Figure 1c) represents a continuous slice of oceanic lithosphere, including ultramafic, mafic, and metasedimentary lithologies, which have been metamorphosed

under eclogite facies conditions during subduction [*Bucher et al*., 2005]. The Zermatt-Saas ophiolite is preserved within a collisional nappe stack, underlain by the Monte Rosa continental basement, and overlain by the Dent Blanche nappe [*Angiboust et al*., 2009]. Twelve metabasaltic and metagabbroic rocks were sampled in three different areas of the complex, which record various *P-T* conditions (Figure 1c): the Pfulwe area located to the east of the town of Zermatt which records a metamorphic climax of 24–26 kbar and 550–600°C [*Bucher et al*., 2005]; the Allalin gabbro which is situated between Zermatt and Saas-Fee and records a metamorphic climax of 2.5 GPa and 610°C [*Bucher and Grapes*, 2009]; and the terminal moraine of the Hohlaub and Allalin glaciers at the Mattmark dam area, which derives from the Allalin gabbro and corresponds to the same peak metamorphic conditions as given for the Allalin gabbro [*Dale et al*., 2007]. These samples are discussed in detail in *Dale et al*. [2007, 2009].

Two different types of metabasalt were collected at Pfulwe. The first of these being samples of eclogitized pillow basalts that comprise garnet, omphacite, quartz, zoisite, paragonite, and phengite. Samples were collected from both the core (S02/75iiiC) and rim (S02/75iiR and S02/75iiiR) of individual pillows. The second type of metabasalt collected at Pfulwe are massive basaltic eclogites (S02/41ii and S02/41v), which comprise garnet, omphacite, glaucophane, epidote, paragonite, and phengite. In addition to the basaltic eclogites, a range of metagabbros from the Allalin and Mattmark areas has also been studied. The three metagabbro samples collected from the Allalin gabbro body display a range in mineralogy. Samples S01/5G and S02/83viiixG consist of olivine, fresh and dusty plagioclase and pyroxene without any evidence of an eclogitic overprint, while sample S01/35iiix is a gabbroic eclogite and is composed of garnet, glaucophane, talc, zoisite, omphacite, paragonite, and rutile. The occurrence of both primary gabbroic and metamorphic eclogitic assemblages within the Allalin metagabbros has been noted before [*Meyer*, 1983; *Dale et al*., 2007; *Bucher and Grapes*, 2009] and is attributed to a combination of the relatively anhydrous nature of the gabbroic protolith, and the short period and only moderate peak temperature of metamorphism. Of the samples collected from the Mattmark moraine, three (S01/40viix, S02/85ixE, and S01/40vx) display typical eclogitic assemblages of coranitic garnet, omphacite, paragonite, glaucophane, phengite, and quartz, while S02/85ixB shows evidence for late retrogression (barroisite, talc, zoisite, and chlorite).

3. Analytical Methods

3.1. Major and Trace Element Concentrations

Samples from Zermatt-Saas have been previously characterized for major and trace element concentrations by *Dale et al*. [2007]. Samples from the Chenaillet and Queyras meta-ophiolites were analyzed for major element concentration by wavelength dispersive X-ray fluorescence at the University of Edinburgh after the method detailed by *Fitton et al*. [1998]. An external international rock standard (USGS BHVO-1) was measured alongside the samples as a check on precision and accuracy. Measured major element values of this geostandard compare well with the average values obtained in Edinburgh ($<$5%) and with accepted values published elsewhere [*Govindaraju*, 1994] ($<$5%). The loss on ignition corrected major element concentrations of the samples and standards analyzed as part of this study are presented in supporting information Table A1.

Trace element concentrations for the Chenaillet and Queyras samples were determined at the National Oceanography Centre, Southampton. Sample powders were digested using concentrated HF and HNO_3 acids, evaporated to dryness and redissolved in 3% HNO_3 spiked with 5 ppb In and Re and 20 ppb Be for use as internal standards. The samples were analyzed on a Thermo X-Series 2 Quadrupole Inductively Coupled Plasma-Mass Spectrometer (ICP-MS), calibrated against five international rock standards, with JA-2 and BHVO-2 run as unknowns. Analysis of these unknowns compare well to the published values, with the external reproducibility being $<$5% for Sc, Ti, V, Ni, Cu, As, Rb, Sr, Y, Cd, Sb, Ba, La, Ce, Nd, Sm, Eu, Gd, Tb, Ho, Tm, Lu, Li, Co, Pr, Dy, Er, and Yb and between 5 and 10% for all other elements. The trace element concentrations are presented in supporting information Table A1.

3.2. Fe Isotope Measurements

The Fe isotope measurements were carried out on whole-rock powders at Durham University. Isotope ratios are reported as δ^{56}Fe in permil notation relative to IRMM-014 external standard, and δ^{57}Fe is given to demonstrate mass dependency of the measurements. All reported errors are 2SD unless stated otherwise.

$$\delta^{56}Fe = (({}^{56}Fe/{}^{54}Fe_{sample})/({}^{56}Fe/{}^{54}Fe_{IRMM-014}) - 1) \times 1000$$

$$\delta^{57}Fe = (({}^{57}Fe/{}^{54}Fe_{sample})/({}^{57}Fe/{}^{54}Fe_{IRMM-014}) - 1) \times 1000$$

The procedure for the chemical separation of Fe is described in detail by *Williams et al*. [2009] but is briefly outlined here. Samples were dissolved using concentrated HF and HNO_3 acids in 7 mL PTFE Teflon square body beakers with wrench top closures in an oven at 165°C for 3 days. These were then further attacked with a 1:1 mix of concentrated HCl and HNO_3 to ensure all refractory phases, such as spinel and rutile, were fully digested. Finally, samples were brought into solution in 6 *M* HCl prior to column chemistry. Quantitative purification of Fe was achieved by chromatographic exchange, using Biorad AG1-X4 anion exchange resin in an HCl medium. All reagents used in the chemistry and mass spectrometry procedures were distilled in subboiling Teflon two-bottle stills at Durham University. The total amount of Fe processed through the columns was typically around 650 μg. The total procedural blank contribution was $<$10 ng of Fe, which is negligible compared to the amount of Fe in the samples. Isotope measurements follow that of *Weyer and Schwieters* [2003] but briefly described here. Measurements were performed by multiple-collector (MC) ICP-MS (Thermo Scientific Neptune Plus) in medium-resolution mode, using an Elemental Scientific Instruments Apex HF desolvating nebulizer for sample introduction. The mass resolution, which is defined as mass/Δmass at 95% and 5% of the beam intensity of the ^{56}Fe peak edge, ranged between 7500 and 9000 depending on daily tuning of the instrument as well as the age of the medium resolution beam slit. At this resolution, it was possible to adequately resolve the $^{40}Ar^{16}O+$, $^{40}Ar^{16}O^{1}H+$, $^{40}Ar^{18}O+$, and $^{40}Ar^{14}N+$ polyatomic species that can interfere on the ^{56}Fe, ^{57}Fe, ^{58}Fe, and ^{54}Fe masses, respectively. Instrumental mass bias was corrected for by sample-standard bracketing, where the beam intensities of the bracketing standard and sample were matched to within 10%. Both sample and standard solutions were run at 2 ppm, giving a beam intensity of between 35 and 50 V on ^{56}Fe, depending on daily sensitivity. In addition to all Fe masses, ^{53}Cr and ^{60}Ni were also monitored and an online Cr and Ni correction was applied to account for any isobaric interferences from ^{54}Cr and ^{58}Ni on the ^{54}Fe and ^{58}Fe masses. These corrections were either negligible or nonexistent due to the effective separation of Fe from Cr and Ni during column chemistry. An in-house standard of $FeCl_2$ was analyzed throughout each analytical sessions giving a mean δ^{56}Fe value of $-0.70 \pm 0.06‰$ and mean δ^{57}Fe value of -1.05 ± 0.06, where $n = 69$, these values are in excellent agreement with previously published measurements of this standard [*Mikutta et al*., 2009]. In addition to this internal standard, an external geostandard, USGS BIR-1, was processed through chemistry and analyzed alongside samples. The BIR-1 analysis gave a mean value of $+0.06 \pm 0.02‰$ for δ^{56}Fe and $+0.08 \pm 0.03‰$ for δ^{57}Fe based on nine measurements from different analytical sessions on the same dissolution. This value is in good agreement with previously published values [*Millet et al*., 2012; *Hibbert et al*., 2012; *Sossi et al*., 2015], which notably were carried out at both high-resolution and low-resolution modes on Nu Plasma and Thermo Neptune instruments.

3.3. Zn Isotope Measurements

The method used for the chemical purification of Zn is based on that of *Moynier et al*. [2006], adapted by *Pons et al*. [2011]. Depending on the Zn concentration of samples, between 30 and 50 mg of rock powder was digested in a 2:1 mix of concentrated HF-HNO_3 in in 7 mL PTFE Teflon square body beakers with wrench top closures in an oven at 165°C for 3 days. As Zn is likely to partition into the fluoride phase as ZnF_2, it is important that all fluorides are fully decomposed prior to column separation, and this was achieved by repeated refluxes of the sample residue in 6 *M* and concentrated HCl. All samples were visually inspected for the presence of fluorides before being evaporated to dryness and brought back into solution in 1.5 *M* HBr, ready for column chemistry.

Quantitative separation of Zn from matrix elements was achieved using Teflon shrink fit columns filled with 0.5 mL of Biorad AG1-X4 anion exchange resin. The resin was cleaned on the column by four repeated passes of 0.5 *M* HNO_3 and Milli-Q (MQ) ultrapure (18.2 MΩ) H_2O, before conditioning in 3 mL of 1.5 *M* HBr. The sample solution was then added to the column and the matrix eluted in 3 mL of 1.5 *M* HBr. Zn was collected from the column in 0.5 *M* HNO_3. To ensure total separation of Zn from matrix elements, this column separation procedure was repeated twice. With the exception of the HBr, which was purchased from ROMIL Ltd. at ultra pure "UpA" grade, all reagents were distilled by subboiling in Teflon stills at Durham University. The total procedural blank is $<$20 ng of Zn, which is negligible compared to the $>$2 μg of sample Zn processed.

Isotope ratio measurements were performed on a Thermo Scientific Neptune Plus MC-ICPMS at Durham University running in low-resolution mode. Samples were introduced via an ESI PFA 50 μL/min nebulizer attached to an ESI cinnabar glass spray chamber. Sample solutions were run at a concentration of 750 ppb Zn in 0.5 *M* HNO_3, this typically gives signal intensities of ~3–4 V on ^{64}Zn. To correct for the effect of instrumental mass bias a combined standard-sample bracketing and empirical external normalization method was adopted. This method applies an external normalization correction [*Maréchal et al*., 1999; *Mason et al*., 2004; *Chen et al*., 2009] by doping both sample and standard solutions with a pure Cu solution (Alfa-Aesar) at a Zn/Cu ratio of 3/1. In addition, each sample analysis was bracketed against measurement of Alfa-Aesar pure Zn standard solution, which had been matched to the same concentration as the sample. During analysis, the masses of ^{63}Cu, ^{64}Zn, ^{65}Cu, ^{66}Zn, ^{67}Zn, and ^{68}Zn were collected, as well as ^{62}Ni to correct, using Ni natural abundances, for ^{64}Ni that is isobaric on ^{64}Zn. In all cases no online or off-line Ni correction was performed, as the calculated contribution of ^{64}Ni to the 64 mass peaks was always lower than 0.5% of the total beam intensity.

The Zn isotope composition of the sample is presented as a delta value in permil notation relative to the JMC-Lyon isotopic standard.

$$\delta^{66}Zn = (({}^{66}Zn/{}^{64}Zn_{sample})/({}^{66}Zn/\delta^{64}Zn_{JMC-Lyon}) - 1) \times 1000$$

Due to a limited supply of the JMC-Lyon standard solution, samples were measured relative to an Alfar-Aesar pure Zn solution. This standard is offset from JMC-Lyon by 0.27‰ for $\delta^{66}Zn$ (2sd = 0.04‰; $n = 87$; over four different analytical sessions); as such we were able to correct our measured value by this factor and present our data relative to JMC-Lyon, as is widely accepted. Precision and accuracy were assessed using the international rock reference material, USGS BCR-2. This rock was processed through chemistry alongside sample powders and measured during analytical sessions. The value obtained for $\delta^{66}Zn$ was +0.30‰ ± 0.04‰ based on five measurements of the same sample aliquot during two analytical sessions. This value agrees well with published results of BCR-2 [*Herzog et al*., 2009; *Moeller et al*., 2012].

4. Results

4.1. Major and Trace Element Data

Major and trace element data for all samples analyzed in this study are given in the supporting information Table A1. With respect to Figures 2b and 2c, it is apparent that the range in Mg# ($[Mg_{Moles}]/([Mg_{Moles}] + [Fe_{Moles}])$) (51–84), MgO (5.6–14.3 wt %), FeO (4.1–9.6 wt %), and Ni (45–385 ppm) is consistent with the fields defined for gabbronorite, gabbro, and olivine gabbro by previous work [*Godard et al*., 2009], with the majority of samples falling within the gabbro field. The Ca# ($[Ca_{Moles}]/([Ca_{Moles}] + [Na_{Moles}])$) of the analyzed samples are lower than those of seafloor oceanic gabbros (Figure 2a), with a range between 36 and 73.

The major element composition of the metasediments (RV5 and CP1) and metasomatic contact zone (CE8a) from Queyras is not shown but presented alongside the data for the metabasalt and metagabbros samples in supporting information Table A1. With the exception of SiO_2, CaO, and Na_2O, the two metasediment samples are broadly similar to estimates of the mean major element composition of global subducted sediments [*Plank and Langmuir*, 1998]. The metasomatic contact zone (CE8a) is best compared directly to metagabbros from the same meta-ophiolite (CE7 and CE12). Relative to these samples CE8a shows depletion in SiO_2 (37.1 wt %), Al_2O_3 (11.3 wt %), CaO (10.4 wt %), K_2O (<0.1 wt %), and Na_2O (2.5 wt %), while it is enriched in Fe_2O_3 (23.9 wt %), TiO_2 (3.9 wt %), MnO (0.4 wt %), and P_2O_5 (0.3 wt %) and a consistent MgO concentration (8.4 wt %).

Trace element data are presented for all of the samples used for this study, grouped by locality, in the form of multielement spidergrams (Figure 3). Where available, relevant published data are presented alongside our sample data for comparison. The Chenaillet metagabbros elemental patterns (PR1 and PR4) are in good agreement with previous studies [e.g., *Chalot-Prat*, 2005] (Figure 3a). They are characterized by a relatively flat trace element profile ($Ce_N/Y_N = 0.8–1.4$; N: primitive mantle normalized), with notable depletions in Li ($Li_N/Y_N = 0.2–0.3$) and an enrichment in Sr ($Sr_N/Nd_N = 1.5–2.9$). The blueschist facies metagabbros (CE7, CE12, QE1, QE10, RV7, TR6, TR9, and BB1) (Figure 3b) and metasomatic contact (CE8a) (Figure 3c) from the Queyras display similar trace element patterns to those of Chenaillet samples, but show significant

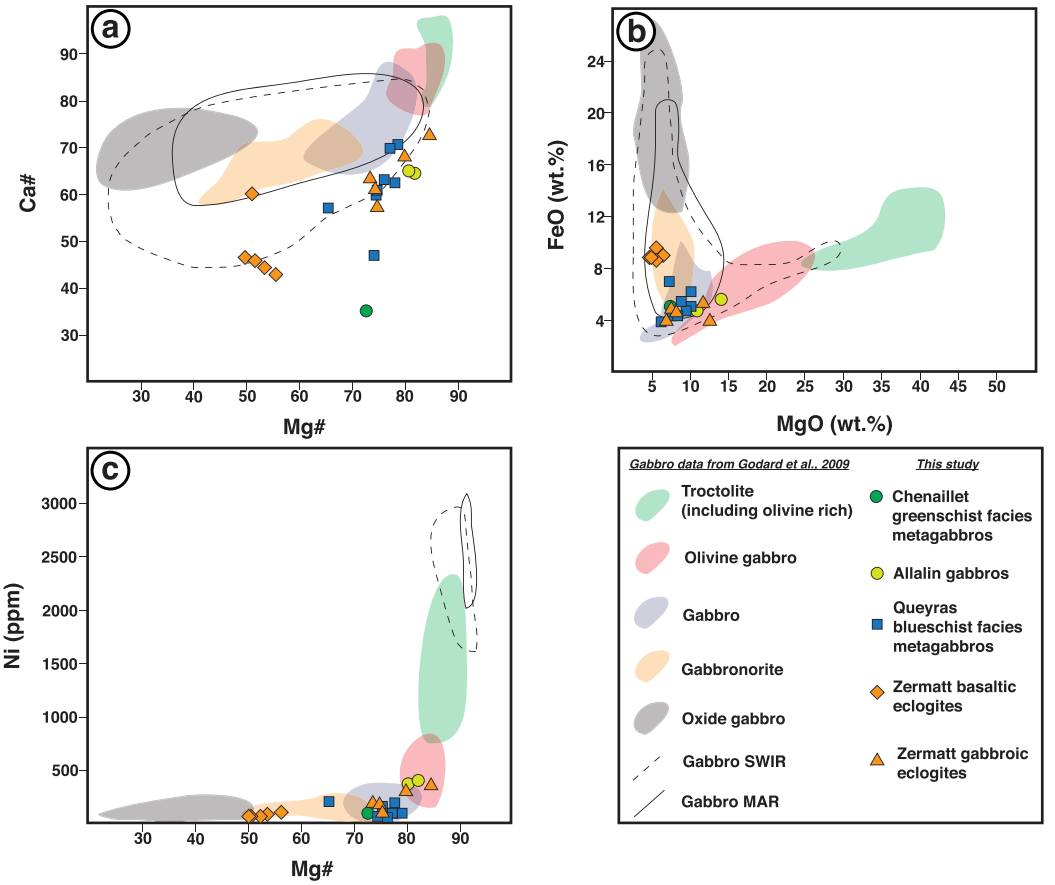

Figure 2. Major element plots of the metagabbroic and metabasaltic samples analyzed as part of this study. The samples are compared to the fields for oceanic gabbros defined by *Godard et al.* [2009]. Ca# is defined as Ca_{TOT} [mol]/Ca_{TOT} [mol] + Na_{TOT} [mol] and Mg# as Mg_{TOT} [mol]/Mg_{TOT} [mol] + Fe_{TOT} [mol]. The field defined by the black dashed line is compiled data from Mid-Atlantic Ridge gabbros, while the field defined by the black solid line is compiled data from South-West Indian Ridge gabbros. Both of these compilations are taken from *Godard et al.* [2009].

enrichment in fluid mobile elements (e.g., Sb_N/Pr_N = 1.3–42.3, B_N/K_N = 1.5–30.5, and Li/Li* = 1.8–25.8; supporting information Table A1).

The trace element profiles for the Zermatt-Saas samples are presented in Figures 3d and 3e. The two samples from the Allalin gabbro are plotted alongside additional data from *Dale et al.* [2007] and compared to the Chenaillet metagabbros (grey field). All of the Allalin gabbros display trace element profiles that are consistent with each other, but are overall of lower concentrations than the patterns of the Chenaillet metagabbros. The trace element profiles are characterized by an enrichment in LREE relative to HREE (La_N/Lu_N = 2.2–3.3), positive anomalies in Sr (Sr_N/Nd_N = 21.3–22), Ba (Ba_N/Th_N = 25.7–49.1), and Eu (Eu_N/Ti_N = 3.5–3.8) and negative anomalies in U (U_N/K_N = 0.1) and Nb (Nb_N/La_N = 0.1). The Zermatt gabbroic eclogites (Figure 3e) display similar trace element patterns to that of the Allalin gabbros (Figure 3d), with positive anomalies in Sr (Sr_N/Nd_N = 2.7–25.5), Eu (Eu_N/Ti_N = 2.2–3.9), and Ba (Ba_N/Th_N = 2–9.5) and depletions in Rb (Rb_N/Ba_N = 0.29–0.3) and Nb (Nb_N/La_N = 0.1–0.4). The basaltic eclogites from Zermatt are shown in Figure 3f. With the exception of K, they show consistent profiles for all elements, this is marked by broadly flay lying profile between LREE to HREE (La_N/Lu_N = 1.5–2.1) and varying depletions in Ba (Ba_N/Th_N = 0.01–0.6), Sr (Sr_N/Nd_N = 0.5–0.7), and Li (Li_N/Y_N = 0.6–1).

4.2. Fe and Zn Stable Isotopes

The whole-rock Fe isotope compositions are reported as δ^{56}Fe and all errors as two standard deviations (2sd) of repeat analyses of the same sample aliquot. The δ^{56}Fe values are presented in the supporting information Table A2. The range of δ^{56}Fe values for all samples analyzed here is between $-0.02 \pm 0.03‰$ and $+0.30 \pm 0.06‰$. The only greenschist facies metagabbro from the Chenaillet that has been analyzed for Fe

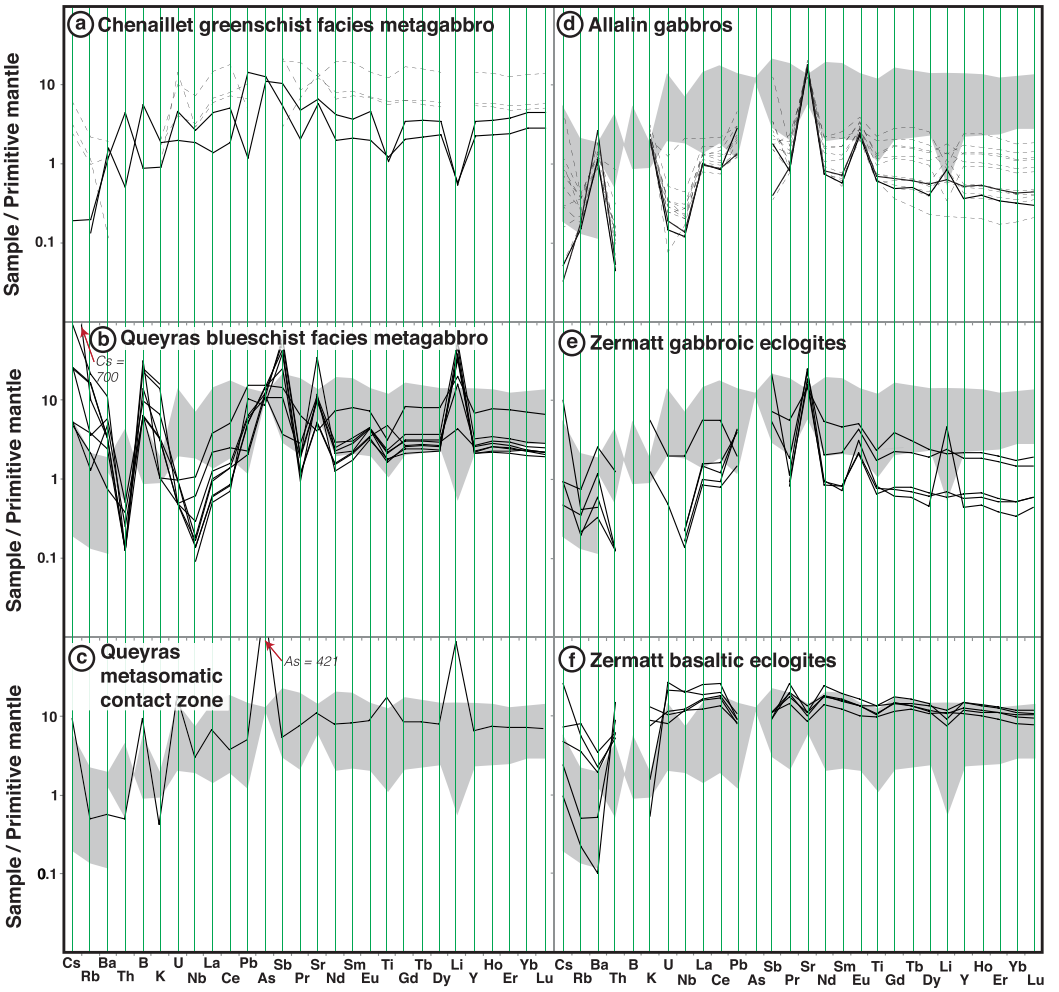

Figure 3. Multielement spidergrams of selected elements for samples analyzed as part of this study. Elements are arranged along the horizontal axis according to degree of compatibility. The grey field shown in Figure 3b–3f outline the "oceanic field" compiled from the Chenaillet metagabbros. Solid black lines denote samples used as part of this study. Dashed black lines represent literature data of comparable samples. The dashed black lines in Figure 3a are metagabbro data for the Chenaillet taken from *Charlot-Prat et al.* [2005], while the dashed black lines in Figure 3d are literature data for the Allalin gabbros taken from *Dale et al.* [2007]. Breaks in the sample profiles indicate elements that were not analyzed. The primitive mantle normalization factors are taken from *McDonough and Sun* [1995].

isotopes (PR4) yields a δ^{56}Fe of $+0.14 \pm 0.06‰$, which is in good agreement with MORB analyzed by *Teng et al.* [2013] and other basaltic rocks [*Sossi et al.*, 2015]. The blueschist facies metagabbros from the Queyras display a range of δ^{56}Fe of between $0.00 \pm 0.06‰$ and $+0.16 \pm 0.04‰$, with no systematic covariation between metamorphic facies. The metasomatic contact zone sample, CE8a, yields the lightest δ^{56}Fe observed: $-0.02 \pm 0.03‰$. The two metasediments from the Queyras, RV5 and CP1 display δ^{56}Fe values of $+0.09 \pm 0.03‰$ and $+0.05 \pm 0.04‰$ respectively. The samples from the Zermatt-Saas ophiolite display the greatest range in Fe isotope composition (δ^{56}Fe $= +0.03 \pm 0.04‰$ to $+0.29 \pm 0.04‰$). Of the two Allalin gabbros selected, one—S02/83viiixG, displays the heaviest δ^{56}Fe value of any of the samples ($+0.30 \pm 0.06‰$), while the other preserves a value indistinguishable from MORB ($+0.11 \pm 0.04‰$). The δ^{56}Fe values of the gabbroic eclogites from Zermatt ranges between $+0.03 \pm 0.04‰$ and $+0.29 \pm 0.04‰$, while the basaltic eclogites show similar δ^{56}Fe values ranging between $+0.05 \pm 0.07‰$ and $+0.18 \pm 0.02‰$.

The zinc isotope composition is reported as δ^{66}Zn, with all errors again being given as 2sd of *n*. The δ^{66}Zn values of all of the samples analyzed here are presented alongside the Fe isotope compositions in the supporting information Table A2. The δ^{66}Zn values of the samples analyzed here ranges from $0.00 \pm 0.02‰$ to $+0.33 \pm 0.03‰$. As with Fe isotopes, there is no covariation between δ^{66}Zn and metamorphic facies. The greenschist facies metagabbro displays a δ^{66}Zn value of $+0.20 \pm 0.04‰$, lower than the suggested MORB

value of $+0.27 \pm 0.03‰$ [*Wang et al.*, 2017]. Significant variation is observed within the blueschist facies metagabbros, which range between $+0.03 \pm 0.02‰$ and $+0.26 \pm 0.03‰$. The metasomatic contact zone from the Queyras has a δ^{66}Zn of $+0.03 \pm 0.02‰$, while the two metasediments show δ^{66}Zn of $0.00 \pm 0.02‰$ to $+0.13 \pm 0.02‰$. Samples from Zermatt display the greatest overall range in δ^{66}Zn, being between $+0.05 \pm 0.03‰$ and $+0.33 \pm 0.03‰$.

5. Discussion

The overall goal of this study is to examine the effects of prograde metamorphism and metasomatism on the Zn and Fe isotope budget of the oceanic crust. To this end we have characterized a suite of metagabbros and metabasalts from three Western Alps ophiolite complexes. These samples display different parageneses from greenschist facies in the Chenaillet massif, representative of seafloor fluid interaction and oceanic crust hydration, to blueschist facies in the Queyras complex, which shows evidence for sediment interaction during subduction, through to high-pressure eclogite facies in the Zermatt-Saas ophiolite. This transect is taken to be representative of *P-T* path for subducting oceanic lithosphere and allows us to assess the effect of subduction zone metamorphism on the mafic portion of the subducting slab [e.g., *Guillot et al.*, 2009; *Schwartz et al.*, 2013]. Furthermore, samples from the Queyras meta-ophiolites were selected as they have previously been demonstrated on the basis of strong enrichments in fluid mobile elements to have been affected by fluid metasomatism from proximal devolatilization of metasedimentary rocks [*Debret et al.*, 2016a].

5.1. The Effect of High-Pressure Metamorphism and Eclogitization of Mafic Lithologies on Fe Isotopes: Zermatt Eclogites

The basaltic eclogites from Zermatt show MORB-like δ^{56}Fe (between 0.07 and 0.14‰) [*Teng et al.*, 2013], ranging between $+0.05$ and $+0.18‰$, with an average of $+0.12 \pm 0.11‰$ (2sd, $n = 5$) suggesting that they retain their primary magmatic composition. To full examine the effect of high-pressure dehydration we present a simple Rayleigh distillation model (shown in supporting information A3), which has been calculated according to the equation below.

$$\delta_{\text{final}} - \delta_{\text{initial}} = (1000 + \delta_{\text{initial}})(F^{(\alpha-1)} - 1)$$

where δ_{final} and δ_{initial} are taken as the average Zermatt basaltic eclogite composition and the average MORB value taken from *Teng et al.* [2013], respectively. The variable F represents the amount of Fe removed from the rock, and α is the fractionation factor between the rock and fluid. Here we have derived the α empirically, choosing to match the modeled δ^{56}Fe to our average measured δ^{56}Fe from the Zermatt basaltic eclogites.

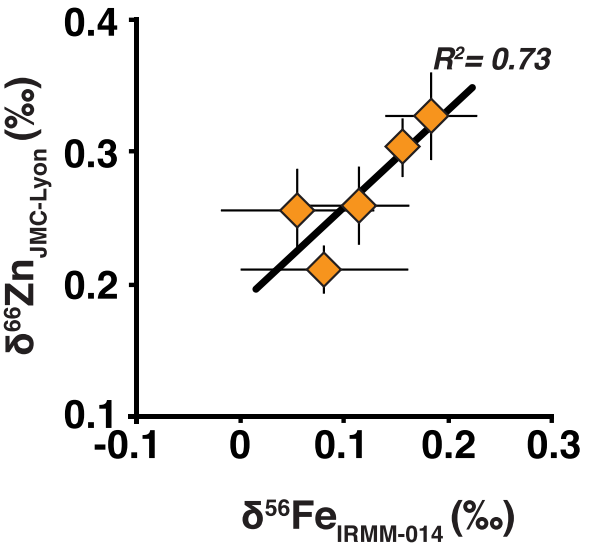

Figure 4. The strong correlation ($R^2 = 0.73$) between the δ^{56}Fe and δ^{66}Zn of the basaltic eclogites from the Zermatt-Saas suggest that both the Fe and Zn stable isotopes composition of these samples is controlled by the same process. All errors are 2sd of the mean of *n*.

Given that the solubility of Fe in aqueous Cl-poor subduction zone fluids is low [*Kessel et al.*, 2004], and considering the relatively small volume of H_2O released during eclogite facies dehydration, it can be taken that the loss of Fe would not exceed 1 wt %. Across the range of possible Fe concentrations (F) we show that the derived fractionation factor is insufficient to significantly perturb the whole-rock Fe isotope composition of the fully dehydrated eclogite, even with the maximum loss of Fe possible. Thus, we suggest that, owing to mass balance constraints, Fe isotopes serve as poor tracers of Fe mobility within these

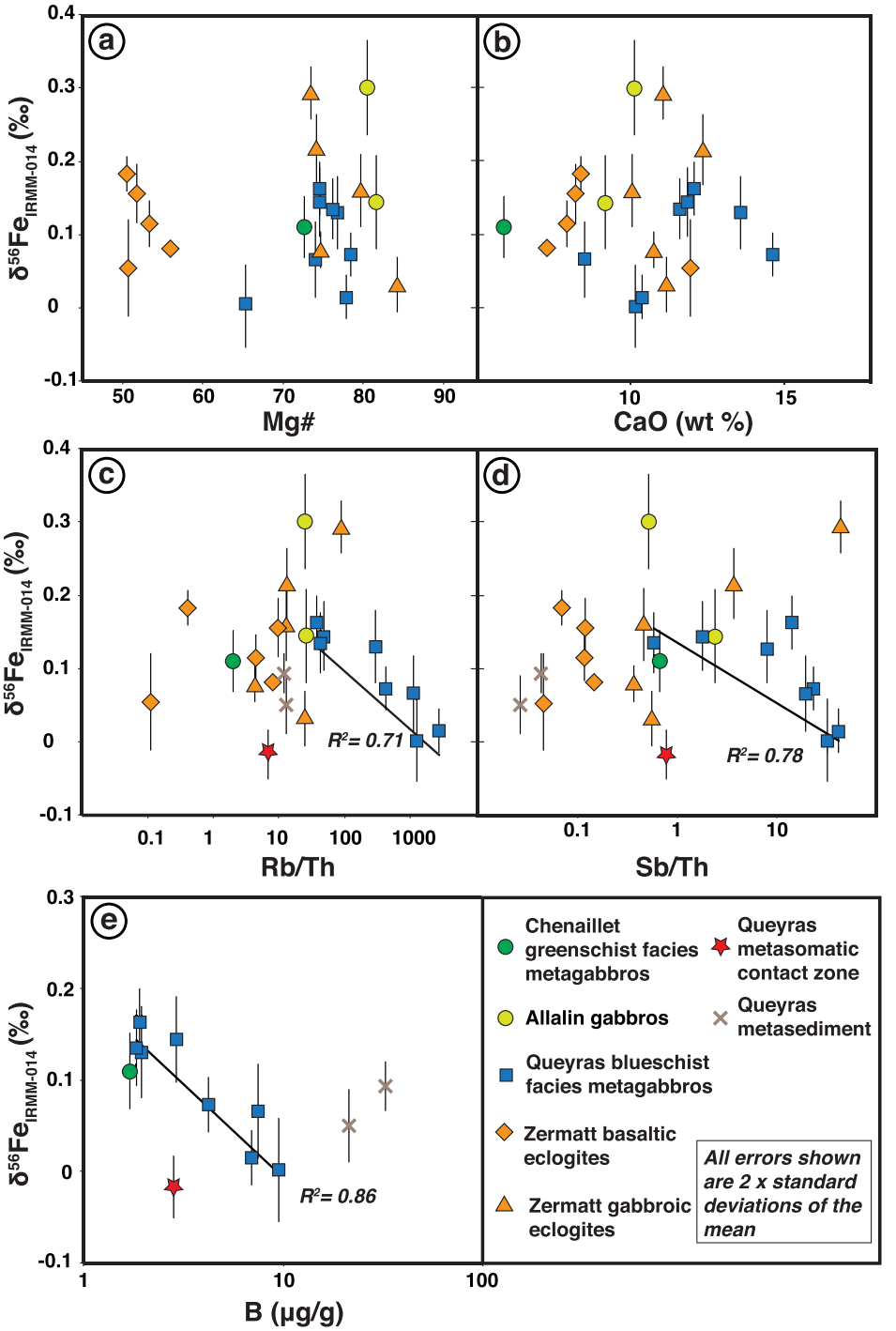

Figure 5. Iron isotope compositions (δ^{56}Fe) plotted against (a, b) indices of magmatic differentiation and (c–e) fluid-rock interaction. The Queyras metasomatic contact zone and the metasediments are not plotted in Figures 5a and 5b as they have not undergone magmatic differentiation. Figures 5c and 5d present ratios of fluid mobile (Rb and Sb) and immobile (Th) elements. The linear regression lines and associated R^2 values plotted in Figures 5c–5e are for the Queyras blueschist metagabbro data only. Boron concentration data were only available for the Chenaillet and Queyras samples. Error bars represent two standard deviations of the mean of *n*.

particular rocks. Similarly the positive correlation ($R^2 = 0.78$) between the δ^{56}Fe and δ^{66}Zn values of basaltic eclogite (Figure 4) suggests that both isotope systems are little affected by prograde metamorphism during subduction. In agreement with this hypothesis, is the observation that δ^{56}Fe and δ^{66}Zn values of the studied eclogitic basalts show a degree of covariation with indices of magmatic differentiation such as Mg# and

CaO (Figure 2), suggesting that both the δ^{56}Fe and δ^{66}Zn in these samples are largely controlled by primary magmatic differentiation.

Many of the Zermatt metagabbro samples display δ^{56}Fe values outside of the range seen in MORB (between 0.07 and 0.14‰) [*Teng et al*., 2013]. Although Fe isotopes can be fractionated in response to magmatic differentiation [*Schuessler et al*., 2009; *Weyer and Seitz*, 2012; *Teng et al*., 2008], there are no systematic covariations between the δ^{56}Fe of the gabbroic eclogites and any indicator of magmatic differentiation (Mg# and CaO) (Figures 5a and 5b). One possible explanation for the level of δ^{56}Fe variation observed is seafloor fluid interaction and alteration of gabbroic oceanic crust, and in particular the incorporation of isotopically light Fe into secondary alteration minerals (including hydrothermal sulfides), which leaves the residual highly altered silicate minerals enriched in heavier Fe isotopes [*Rouxel et al*., 2003]. Although this could account for such isotopic compositions, the absence of chalcophile element enrichment within the whole rock make it unlikely that these lithologies have been affect by hydrothermal alteration and the formation of secondary sulfides. Another possibility is that Fe isotope fractionation took place during prograde metamorphism and associated metasomatism or dehydration of the Zermatt metagabbro protoliths. However, no covariation between metamorphic grade and Fe isotope composition is observed. It should be noted, however, that the gabbroic eclogite with the heaviest δ^{56}Fe (S02/85ixB) shows the most evidence for blueschist facies retrogression, and it is possible that retrograde processes could have modified the δ^{56}Fe of these samples.

5.2. Fe Isotope Fractionation in Response to Fluid Metasomatism at Blueschist Facies: The Queyras Meta-Ophiolites

A single metagabbro sample from the Chenaillet possesses a δ^{56}Fe value of $+0.11 \pm 0.04$‰, which is in good agreement with published values obtained for MORB of between $+0.11$ and $+0.17$‰ [*Teng et al*., 2013]. The blueschist metagabbros from the Queyras meta-ophiolites display a similar range of Fe isotope compositions to the gabbroic eclogites from Zermatt but, on average are offset toward lighter δ^{56}Fe values, with a mean δ^{56}Fe of $+0.09 \pm 0.12$‰, (2sd, $n = 8$) as opposed to $+0.16 \pm 0.21$‰, (2sd, $n = 5$) for the Zermatt gabbroic eclogites.

A notable feature of the samples from the Queyras is the substantial enrichment in fluid mobile elements, such as Rb, B, Sb, and Li (Figure 3b). This enrichment is thought to result from fluid infiltration from the surrounding metasediments and the incorporation of fluid mobile elements during recrystallization under blueschist facies conditions. This type of high-pressure interaction between external fluids and surrounding lithologies, which results in the enrichment in fluid mobile elements has been noted elsewhere globally [*Marschall et al*., 2009; *Penniston-Dorland et al*., 2012; *Vitale Brovarone and Beyssac*, 2014]. Consequently, it is possible to use these samples to document the effect of high-pressure fluid infiltration during subduction on the behavior of Fe (and Zn) isotopes. Owing g to the low solubility of, Th and B relative to Rb and Sb in aqueous fluids [e.g., *Kessel et al*., 2005; *Zack and John*, 2007], we have used the ratios of Rb/Th and Sb/Th alongside elemental concentrations of B in these samples as an indicator of fluid-rock interaction occurring during subduction. A negative correlation is observed between indices of fluid-rock interaction (Rb/Th, Sb/Th, and B) and the δ^{56}Fe values of the samples (Figures 5c–5e). This correlation provides evidence for a relationship between fluid infiltration and Fe isotope systematics in the blueschist facies metagabbros in the Queyras. The perturbation of the bulk rock δ^{56}Fe by an external fluid can be accounted for by two possible mechanisms: (1) isotopically heavy Fe is preferentially complexed into the fluid and lost from the metagabbros, leaving the residual rock enriched in light Fe isotopes or (2) isotopically light Fe is transported via the external fluid and incorporated into one or more of the blueschist facies minerals that make up the metagabbros, thus enriching the bulk rock in light Fe isotopes. Mechanism 1, the loss of isotopically heavy Fe, appears unlikely, because previous work has demonstrated the preferential mobility of isotopically light Fe in slab derived dehydration fluids [*Debret et al*., 2016b]. Specifically, it would be expected that the heavy isotopes of Fe would have a preference for Fe^{3+} complexes [*Polyakov and Mineev*, 2000], and the solubility of Fe^{3+} relative to Fe^{2+} in aqueous solution is known to be low [*Ding and Seyfried*, 1992]. Consequently, it seems much more likely that the light Fe isotope composition of the metagabbros is caused by the incorporation of externally derived low-δ^{56}Fe fluids (mechanism 2).

Fluids can acquire distinctively light Fe isotope compositions through different means. These include kinetic processes (i.e., enhanced mobility of isotopically light Fe); preferential dissolution of low-δ^{56}Fe phases; or, equilibrium partitioning, where isotopically light Fe is preferentially complexed by aqueous SO_X [*Hill et al*., 2010] and Cl [*Testemale et al*., 2009] ligands, as suggested to be the case for Western Alps subducted

serpentinites [*Debret et al*., 2016b]. Because there is no observed covariation between the δ^{56}Fe and δ^{66}Zn of the blueschist facies metagabbros, we suggest that kinetic processes are not responsible, as if this was to be the case we would expect to see the two systems covary accordingly. Alternatively, it could be considered that preferential dissolution of a low-δ^{56}Fe phase within the sediments, such as a sulfide, could result in an isotopically light metasomatizing fluid. The metasediments analyzed here do show isotopically light Fe isotope compositions relative to the metagabbros from the same area, but show no evidence of sulfur bearing phase dissolution (supporting information A1 and A2). In order to test this further, we have applied a simple mass balance calculation using the equation shown below.

$$\delta^{56}\mathrm{Fe}_{\mathrm{mixture}} = (([\mathrm{Fe}]_{\mathrm{rock}} \times \delta^{56}\mathrm{Fe}_{\mathrm{rock}}) + ([\mathrm{Fe}]_{\mathrm{fluid}} \times \delta^{56}\mathrm{Fe}_{\mathrm{fluid}}))/([\mathrm{Fe}]_{\mathrm{rock}} \times [\mathrm{Fe}]_{\mathrm{fluid}})$$

If we were to take the sediment composition as being representative of the fluid compositions, then mass balance suggests that we would have to add near ~60% of the sediment to the metagabbro reservoir to generate the lightest δ^{56}Fe observed. As this is unrealistic, we can only suggest that the Fe isotope composition of the bulk sediments analyzed does not reflect that of the fluid. Hence, we are unable to precisely identify which reaction in the metasedimentary rocks could generate a fluid with an isotopically light Fe signature. Hydrothermal fluids from mid-ocean ridges are known to be isotopically light with respect to Fe [*Rouxel et al*., 2003, 2008; *Beard et al*., 2003], if we were to assume that these fluids are representative of the type of fluids cycling in subduction zones, and that have been responsible for metasomatizing the metagabbros in the Queyras, the mass balance suggests that addition of ~20% fluid with a δ^{56}Fe of $-0.5‰$ to the metagabbro could account for the light δ^{56}Fe observed. The role of infiltrating fluids derived from other lithologies such as serpentinites could also be considered here. Indeed, it has been shown that the devolatilization of serpentinized ultramafic rocks can release fluids enriched in isotopically light Fe and heavy Zn, interpreted to reflect the release of sulfate-bearing fluids during serpentinite devolatilization [*Debret et al*., 2016b; *Pons et al*., 2016]. If such fluids were to be released from proximal serpentinite bodies in the Queyras, and be the key metasomatic agent for the metagabbros here then we would expect to see a consistent, coupled Fe and Zn isotope variation. As we only see the process of fluid metasomatism reflected in the Fe isotope composition of the metagabbros, then we can only suggest that the fluids, and associated isotopically light Fe originates from the sediments.

5.3. Zn Isotope Systematics of Metabasalts and Metagabbros From the Queyras and Zermatt-Saas Ophiolites

The igneous samples (metabasalts and metagabbros) analyzed here possess δ^{66}Zn isotope compositions that range from $+0.03 \pm 0.02‰$ to $+0.30 \pm 0.02‰$, with a mean δ^{66}Zn value of $+0.21 \pm 0.16‰$ (2sd; $n = 21$). Recent work by *Wang et al*. [2017] suggests that MORB possesses a Zn isotope composition of $\delta^{66}\mathrm{Zn} = +0.28 \pm 0.03‰$ ($n = 6$; samples from Carlsberg and North Atlantic), which is indistinguishable within error of the studied samples. The absence of any variation between Zn concentration and δ^{66}Zn within the sample set suggests that the overall δ^{66}Zn is not the result of Zn mobility during fluid loss under eclogite facies conditions. To demonstrate this we have modeled the evolution of δ^{66}Zn within the dehydrated eclogite according to the same Rayleigh distillation equation given in section 5.1, the result of which is shown in the supporting information A4. This model confirms that the solubility of Zn, even in the presence of aqueous SO_x and/or CO_x species, is too low to lead to a significant fractionation of zinc isotopes in the metabasaltic eclogites during prograde metamorphism.

In the case of the Queyras blueschist facies metagabbros, the lack of a correlation between δ^{66}Zn and fluid mobile elements (supporting information A5), suggests that the blueschist facies sediment interaction, which has affected Fe isotopes, has not perturbed the whole-rock Zn isotope systematics of these samples. However, it is possible that the external metasomatic fluid either possesses Zn concentrations that are too low to significantly affect the Zn isotope composition of the metagabbros, or else that the sediment derived fluid preserves a Zn isotope composition indistinguishable to that of the metagabbros, and owing to the mass balance this interaction is not traceable with Zn isotopes. It is notable that the metasomatic contact between metagabbros and metasedimentary rocks analyzed here preserves the lightest δ^{66}Zn ($+0.03 \pm 0.02‰$) and δ^{56}Fe ($-0.02 \pm 0.03‰$) values. Previous studies have shown that kinetic fractionation can occur along such type of metasomatic interfaces [*Teng et al*., 2006; *Marschall et al*., 2007; *Penniston-Dorland et al*., 2010; *Pogge von Strandman et al*., 2015] resulting in a decrease of isotopic values. These compositions arise from a preferential diffusive partitioning of the lighter isotopes relative to the heavier isotopes. It is thus conceivable that similar processes locally occur in the Queyras, however, further work would be required to comment on this conclusively.

Recently Zn isotopes have been shown to be sensitive to mantle partial melting [*Doucet et al*., 2016; *Wang et al*., 2017] and igneous differentiation [*Chen et al*., 2013], but owing to the complex metasomatic and metamorphic history of the studied samples, coupled with the lack of a comprehensive study of Zn isotopes in global MORB and oceanic gabbros, it is difficult to conclude if the variations in Zn isotope composition observed here reflect primary magmatic process or modification by late stage alteration and metasomatic processes. While it has previously been stated that the process of low-temperature seafloor alteration of the upper, basaltic oceanic lithosphere has little effect on Zn isotopes, the same study demonstrated that high-temperature (>350°C) hydrothermal circulation and complexing of light Zn isotopes in hydrothermal fluids could drive the Zn isotope composition toward heavier δ^{66}Zn values in the gabbroic portion of the oceanic lithosphere [*Huang et al*., 2016]. This observation could be invoked to explain the range of δ^{66}Zn values observed in the Zermatt and Queyras metagabbros, but as the samples now preserve a subduction-related, Alpine overprint to their mineralogy it is not possible to unambiguously conclude on the effect of seafloor hydrothermal activity on the Zn isotope compositions of these rocks.

5.4. Implications for Slab Dehydration and the Redox Budget of the Subarc Mantle

Mass transfer from the subducted slab can be considered with respect to three components: sediments; mafic oceanic crust, and the serpentinized slab mantle. Of these, the serpentinized slab mantle has received much attention as the main carrier of fluids into subduction zones, as hydrated peridotite can contain up to 13 wt % H_2O [*Ulmer and Trommsdorff*, 1995]. Indeed, the prograde dehydration of subducting serpentinites has been demonstrated to contribute significantly to the fluid budget of the subarc mantle [*Scambelluri and Tonarini*, 2012]. When considered with the findings of *Debret et al*. [2016b] and *Pons et al*. [2016], who show clear fractionation of both Fe and Zn stable isotopes with increasing subduction metamorphism, it is likely that serpentinite-derived fluids, in combination with sediment melts, exert a strong control on the transfer of redox mediating elements between the slab and overlying subarc-arc. This is consistent with the results of many studies that have highlighted the importance of distinct contributions from serpentinite-derived slab fluids and sediment melts in the source regions of arc lavas [e.g., *Plank and Langmuir*, 1993; *Elliott et al*., 1997; *Freymuth et al*., 2015; *Nebel et al*., 2015; *Sossi et al*., 2016].

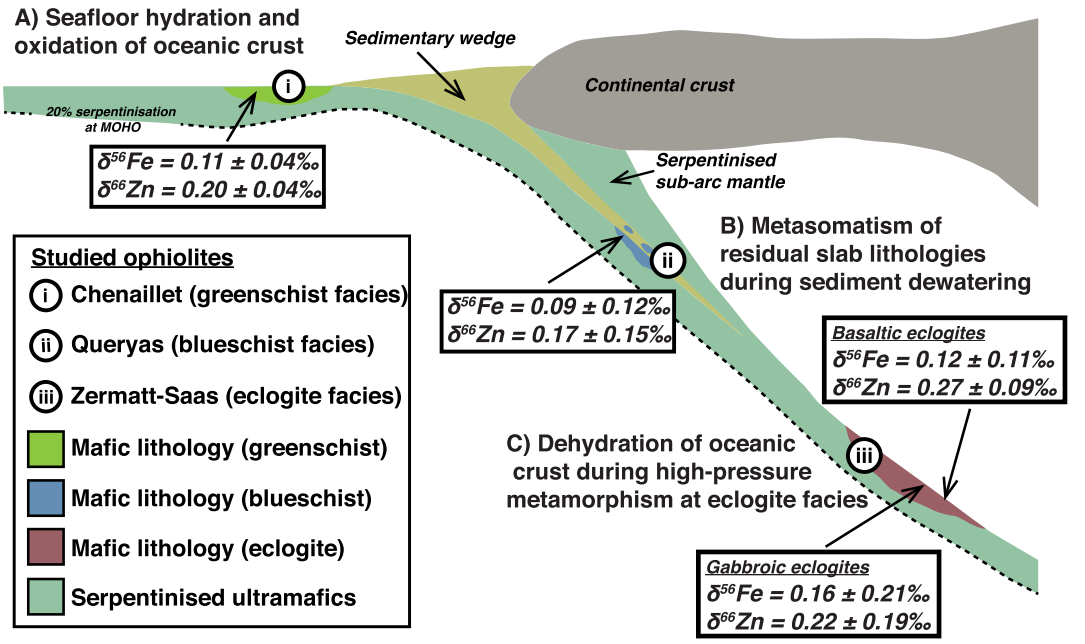

Figure 6. Schematic diagram (modified after *Debret et al*. [2016a]) showing the approximate location of the meta-ophiolites studied as part of this work: (i) Chenaillet massif; (ii) Queyras complex; and (iii) Zermatt-Saas ophiolite. Each of these meta-ophiolites has been metamorphosed under conditions representative of a subduction gradient (greenschist to blueschist to eclogite) and allows us to examine the effect of slab metamorphism and metasomatism on the mafic oceanic crust. For each of these ophiolites, the average δ^{56}Fe and δ^{66}Zn values are presented.

We have demonstrated that the effect of high-pressure subduction zone metamorphism and associated dehydration at eclogite facies, has no detectable effect on the whole-rock Fe and Zn stable isotope composition of subducted metabasalts and metagabbros (Figure 6). This is significant with respect to two aspects. First, we show that an absence of resolvable Fe isotope variation at eclogite facies, with respect to a MORB protolith, demonstrates that Fe isotopes are not fractionated in response to loss of Fe during dehydration of mafic lithologies in subduction Secondly we show that Zn isotopes remain unfractionated, suggesting that the dehydration fluids released by the process of eclogitization are not major carriers of aqueous Zn-SO_X and/or Zn-CO_X complexes.

The results from this study, at least, suggest that high-pressure subduction zone metamorphism has no detectable effect on Fe or Zn isotope composition of the mafic lithologies within the subducting slab. Consequently, the mafic slab component that is recycled back into the mantle preserves a MORB-like Fe and Zn isotope signature.

6. Conclusions

We have analyzed a suite of metagabbros and metabasalts, which have been metamorphosed under the different conditions of a subduction zone gradient, and are taken to be representative of the mafic oceanic crust during subduction. Our data show that fluids released from subducting sediments can interact and metasomatize mafic slab lithologies. This metasomatism is capable of modifying bulk rock Fe isotope composition, with the samples displaying the most evidence for fluid interaction recording the lightest Fe isotope compositions. This is likely due to the incorporation of an isotopically light Fe component, which is derived from the associated subducted sediments. Within the same samples zinc isotopes show no evidence of being perturbed by this metasomatic process. Consequently, we conclude that Fe isotopes in subducting oceanic crust are sensitive tracers of slab metasomatism, relating to fluid released from subducting sediments.

Contrary to this it is apparent that no systematic variation in isotopic composition across metamorphic grade is observed, suggesting that the mobility of Fe during the dehydration of the mafic lithologies in subduction zones is too low to lead to significant isotopic variations within the dehydrated lithologies. Additionally our Zn isotope data demonstrate that the fluids released by these dehydration reactions are not major carriers of dissolved Zn-SO_X/CO_X complexes.

Acknowledgments
This work was supported by an ERC Starting grant (HabitablePlanet; 306655) and a NERC Deep Volatiles Consortium grant (NE/M0003/1) awarded to H.W. B.D. and M.L.P. were supported as PDRAs on the HabitablePlanet grant, while the PhD studentship to E.I. was funded as part of the same project. PB acknowledges support from ERC Starting Grant (MASE; 279828), and his Auvergne Fellowship (French Government Laboratory of Excellence initiative no. ANR-10-LABX-0006; ClerVolc contribution no. 253). M.A.M. was funded by a Durham University International Junior Fellowship. Careful and constructive reviews from Oliver Nebel, Paolo Sossi, Horst Marschall, and an anonymous reviewer greatly improved the quality of this manuscript. Janne Blichert-Toft is also acknowledged for her patient editorial handling. We thank Christian Nicollet (LMV, Clermont-Ferrand, France) for discussions in the field and for providing the metagabbro samples from the Queyras and Chenaillet ophiolites. The full major and trace element composition of all of the samples presented in this study can be found within the supporting information. The Fe and Zn isotope data are also included within the supporting information.

References

Angiboust, S., P. Agard, L. Jolivet, and O. Beyssac (2009), The Zermatt-Saas ophiolite: The largest (60-km wide) and deepest (c. 70–80 km) continuous slice of oceanic lithosphere detached from a subduction zone?, *Terra Nova*, *21*(3), 171–180.

Beard, B. L., C. M. Johnson, K. L. Von Damm, and R. L. Poulson (2003), Iron isotope constraints on Fe cycling and mass balance in oxygenated Earth oceans, *Geology*, *31*(7), pp. 629–632.

Bernoulli, D., G. Manatschal, L. Desmurs, and O. Muntener (2003), Where did Gustav Steinmann see the trinity? Back to the roots of an Alpine ophiolite concept, *Geol. Soc. Am. Spec. Pap.*, *373*, 93–110.

Black, J. R., A. Kavner, and E. A. Schauble (2011), Calculation of equilibrium stable isotope partition function ratios for aqueous zinc complexes and metallic zinc, *Geochim. Cosmochim. Acta*, *75*(3), 769–783.

Bouilhol, P., V. Magni, J. van Hunen, and L. Kaislaniemi (2015), A numerical approach to melting in warm subduction zones, *Earth Planet. Sci. Lett.*, *411*, 37–44.

Brandon, A. D., and D. S. Draper (1996), Constraints on the origin of the oxidation state of mantle overlying subduction zones: An example from Simcoe, Washington, USA, *Geochim. Cosmochim. Acta*, *60*(10), 1739–1749.

Brouwer, F. M., D. M. A. Van De Zedde, M. J. R. Wortel, and R. L. M. Vissers (2004), Late-orogenic heating during exhumation: Alpine PTt trajectories and thermomechanical models, *Earth Planet. Sci. Lett.*, *220*(1), 185–199.

Bucher, K., and R. Grapes (2009), The eclogite-facies Allalin Gabbro of the Zermatt–Saas ophiolite, Western Alps: A record of subduction zone hydration, *J. Petrol.*, *50*(8), 1405–1442.

Bucher, K., Y. Fazis, C. D. Capitani, and R. Grapes (2005), Blueschists, eclogites, and decompression assemblages of the Zermatt-Saas ophiolite: High-pressure metamorphism of subducted Tethys lithosphere, *Am. Mineral.*, *90*(5–6), 821–835.

Caby, R. (1995), Plastic deformation of gabbros in a slow-spreading Mesozoic ridge: Example of the Montgenevre ophiolite, Western Alps, in *Mantle and Lower Crust Exposed in Oceanic Ridges and in Ophiolites*, pp. 123–145, Springer, Netherlands.

Chalot-Prat, F. (2005), An undeformed ophiolite in the Alps: Field and geochemical evidence for a link between volcanism and shallow plate tectonic processes, *Geol. Soc. Am. Spec. Pap.*, *388*, 751–780.

Chen, H., P. S. Savage, F. Z. Teng, R. T. Helz, and F. Moynier (2013), Zinc isotope fractionation during magmatic differentiation and the isotopic composition of the bulk Earth, *Earth Planet. Sci. Lett.*, *369*, 34–42.

Chen, J., J. Gaillardet, P. Louvat, and S. Huon (2009), Zn isotopes in the suspended load of the Seine River, France: Isotopic variations and source determination, *Geochim. Cosmochim. Acta*, *73*(14), 4060–4076.

Dale, C. W., A. Gannoun, K. W. Burton, T. W. Argles, and I. J. Parkinson (2007), Rhenium–osmium isotope and elemental behaviour during subduction of oceanic crust and the implications for mantle recycling, *Earth Planet. Sci. Lett.*, *253*(1), 211–225.

Dale, C. W., K. W. Burton, D. G. Pearson, A. Gannoun, O. Alard, T. W. Argles, and I. J. Parkinson (2009), Highly siderophile element behaviour accompanying subduction of oceanic crust: Whole rock and mineral-scale insights from a high-pressure terrain, *Geochim. Cosmochim. Acta*, *73*(5), 1394–1416.

Dauphas, N., P. R. Craddock, P. D. Asimow, V. C. Bennett, A. P. Nutman, and D. Ohnenstetter (2009), Iron isotopes may reveal the redox conditions of mantle melting from Archean to Present, *Earth Planet. Sci. Lett.*, *288*(1), 255–267.

Dauphas, N., M. Roskosz, E. E. Alp, D. R. Neuville, M. Y. Hu, C. K. Sio, and F. L. H. Tissot (2014), Magma redox and structural controls on iron isotope variations in Earth's mantle and crust, *Earth Planet. Sci. Lett.*, *398*, 127–140.

Debret, B., C. Nicollet, M. Andreani, S. Schwartz, and M. Godard (2013), Three steps of serpentinization in an eclogitized oceanic serpentinization front (Lanzo Massif–Western Alps), *J. Metamorph. Geol.*, *31*(2), 165–186.

Debret, B., K. T. Koga, F. Cattani, C. Nicollet, G. Van den Bleeken, and S. Schwartz (2016a), Volatile (Li, B, F and Cl) mobility during amphibole breakdown in subduction zones, *Lithos*, *244*, 165–181.

Debret, B., M. A. Millet, M. L. Pons, P. Bouilhol, E. Inglis, and H. Williams (2016b), Isotopic evidence for iron mobility during subduction, *Geology*, *44*(3), 215–218.

Ding, K., and W. E. Seyfried (1992), Determination of Fe-Cl complexing in the low pressure supercritical region (NaCl fluid): Iron solubility constraints on pH of subseafloor hydrothermal fluids, *Geochim. Cosmochim. Acta*, *56*(10), 3681–3692.

Doucet, L. S., N. Mattielli, D. A. Ionov, W. Debouge, and A. V. Golovin (2016), Zn isotopic heterogeneity in the mantle: A melting control?, *Earth Planet. Sci. Lett.*, *451*, 232–240.

Elliott, T., T. Plank, A. Zindler, W. White, and B. Bourdon (1997), Element transport from slab to volcanic front at the Mariana arc, *J. Geophys. Res.*, *102*(B7), 14,991–15,019.

Evans, B. W., V. Trommsdorff, and W. Richter (1979), Petrology of an eclogite-metarodingite suite at Cima di Gagnone, Ticino, Switzerland, *Am. Mineral.*, *64*(1–2), 15–31.

Evans, K. A. (2012), The redox budget of subduction zones, *Earth Sci. Rev.*, *113*(1), 11–32.

Fitton, J. G., A. D. Saunders, L. M. Larsen, B. S. Hardarson, and M. J. Norry (1998), Volcanic rocks from the southeast Greenland margin at 63°N: composition, petrogenesis, and mantle sources, edited by A. D. Saunders, H. C. Larsen, and S. W. Wise, Jr., pp. 331–350, *Proc. ODP, Sci. Results*, 152, Ocean Drill. Program, College Station, Tex.

Foley, S. F., M. G. Barth, and G. A. Jenner (2000), Rutile/melt partition coefficients for trace elements and an assessment of the influence of rutile on the trace element characteristics of subduction zone magmas, *Geochim. Cosmochim. Acta*, *64*(5), 933–938.

Freymuth, H., F. Vils, M. Willbold, R. N. Taylor, and T. Elliott (2015), Molybdenum mobility and isotopic fractionation during subduction at the Mariana arc, *Earth Planet. Sci. Lett.*, *432*, 176–186.

Frezzotti, M. L., J. Selverstone, Z. D. Sharp, and R. Compagnoni (2011), Carbonate dissolution during subduction revealed by diamond-bearing rocks from the Alps, *Nat. Geosci.*, *4*(10), 703–706.

Frost, B. R., and C. Ballhaus (1998), Comment on "Constraints on the origin of the oxidation state of mantle overlying subduction zones: An example from Simcoe, Washington, USA" by A. D. Brandon and D. S. Draper, *Geochim. Cosmochim. Acta*, *62*, 329–332.

Fujii, T., F. Moynier, M. L. Pons, and F. Albarède (2011), The origin of Zn isotope fractionation in sulfides, *Geochim. Cosmochim. Acta*, *75*(23), 7632–7643.

Godard, M., et al. (2009), Geochemistry of a long in-situ section of intrusive slow-spread oceanic lithosphere: Results from IODP Site U1309 (Atlantis Massif, 30 N Mid-Atlantic-Ridge), *Earth Planet. Sci. Lett.*, *279*(1), 110–122.

Govindaraju, K. (1994), Compilation of working values and sample descriptions for 383 geostandards, *Geostand. Newsl.*, *18*, 1–55.

Guillot, S., K. Hattori, P. Agard, S. Schwartz, and O. Vidal (2009), Exhumation processes in oceanic and continental subduction contexts: A review, in *Subduction Zone Geodynamics*, pp. 175–205, Springer, Berlin Heidelberg.

Hawkesworth, C. J., K. Gallagher, J. M. Hergt, and F. McDermott (1993), Mantle and slab contribution in arc magmas, *Annu. Rev. Earth Planet. Sci.*, *21*, 175–204.

Hensen, C., K. Wallmann, M. Schmidt, C. R. Ranero, and E. Suess (2004), Fluid expulsion related to mud extrusion off Costa Rica—A window to the subducting slab, *Geology*, *32*(3), 201–204.

Hermann, J., and D. H. Green (2001), Experimental constraints on high pressure melting in subducted crust, *Earth Planet. Sci. Lett.*, *188*(1), 149–168.

Hermann, J., O. Müntener, and M. Scambelluri (2000), The importance of serpentinite mylonites for subduction and exhumation of oceanic crust, *Tectonophysics*, *327*(3), 225–238.

Hermann, J., C. Spandler, A. Hack, and A. V. Korsakov (2006), Aqueous fluids and hydrous melts in high-pressure and ultra-high pressure rocks: Implications for element transfer in subduction zones, *Lithos*, *92*(3), 399–417.

Herzog, G. F., F. Moynier, F. Albarède, and A. A. Berezhnoy (2009), Isotopic and elemental abundances of copper and zinc in lunar samples, Zagami, Pele's hairs, and a terrestrial basalt, *Geochim. Cosmochim. Acta*, *73*(19), 5884–5904.

Hibbert, K. E. J., H. M. Williams, A. C. Kerr, and I. S. Puchtel (2012), Iron isotopes in ancient and modern komatiites: Evidence in support of an oxidised mantle from Archean to present, *Earth Planet. Sci. Lett.*, *321*, 198–207.

Hill, P. S., E. A. Schauble, and E. D. Young (2010), Effects of changing solution chemistry on Fe^{3+}/Fe^{2+} isotope fractionation in aqueous Fe–Cl solutions, *Geochim. Cosmochim. Acta*, *74*(23), 6669–6689.

Huang, J., S.-A. Liu, Y. Gao, Y. Xiao, and S. Chen (2016), Copper and zinc isotope systematics of altered oceanic crust at IODP Site 1256 in the eastern equatorial Pacific, *J. Geophys. Res. Solid Earth*, *121*, 7086–7100, doi:10.1002/2016JB013095.

Kelley, K. A., and E. Cottrell (2009), Water and the oxidation state of subduction zone magmas, *Science*, *325*(5940), 605–607.

Kessel, R., P. Ulmer, T. Pettke, M. W. Schmidt, and A. B. Thompson (2004), A novel approach to determine high-pressure high-temperature fluid and melt compositions using diamond-trap experiments, *Am. Mineral.*, *89*(7), 1078–1086.

Kessel, R., M. W. Schmidt, P. Ulmer, and T. Pettke (2005), Trace element signature of subduction-zone fluids, melts and supercritical liquids at 120–180 km depth, *Nature*, *437*(7059), 724–727.

Konter, J. G., A. J. Pietruszka, B. B. Hanan, V. A. Finlayson, P. R. Craddock, M. G. Jackson, and N. Dauphas (2016), Unusual δ^{56}Fe values in Samoan rejuvenated lavas generated in the mantle, *Earth Planet. Sci. Lett.*, *450*, 221–232.

Lagabrielle, Y., and M. Cannat (1990), Alpine Jurassic ophiolites resemble the modern central Atlantic basement, *Geology*, *18*(4), 319–322.

Lagabrielle, Y., et al. (1984), Les témoins d'une tectonique intra-océanique dans le domaine téthysien: Analyse des rapports entre les ophiolites et leurs couvertures métasédimentaires dans la zone piémontaise des Alpes franco-italiennes, *Ofioliti*, *9*, 67–88.

Lagabrielle, Y., S. Fudraland, and J. R. Kienast (1990), La couverture océanique des ultrabasites de Lanzo (Alpes occidentales): Arguments lithostratigraphiques et pétrologiques, *Geodin. Acta*, *4*(1), 43–55.

Lagabrielle, Y., A. Vitale Brovarone, and B. Ildefonse (2015), Fossil oceanic core complexes recognized in the blueschist metaophiolites of Western Alps and Corsica, *Earth Sci. Rev.*, *141*, 1–26.

Lemoine, M., P. Tricart, and G. Boillot (1987), Ultramafic and gabbroic ocean floor of the Ligurian Tethys (Alps, Corsica, Apennines): In search of a genetic imodel, *Geology*, *15*(7), 622–625.
Magni, V., P. Bouilhol, and J. van Hunen (2014), Deep water recycling through time, *Geochem. Geophys. Geosyst.*, *15*, 4203–4216, doi: 10.1002/2014GC005525.
Manatschal, G., D. Sauter, A. M. Karpoff, E. Masini, G. Mohn, and Y. Lagabrielle (2011), The Chenaillet ophiolite in the French/Italian Alps: An ancient analogue for an oceanic core complex?, *Lithos*, *124*(3), 169–184.
Maréchal, C. N., P. Télouk, and F. Albarède (1999), Precise analysis of copper and zinc isotopic compositions by plasma-source mass spectrometry, *Chem. Geol.*, *156*(1), 251–273.
Marschall, H. R., P. A. E. Pogge von Strandmann, H.-M. Seitz, T. Elliott, and Y. Niu (2007), The lithium isotopic composition of orogenic eclogites and deep subducted slabs, *Earth Planet. Sci. Lett.*, *262*(3), 563–580.
Marschall, H. R., R. Altherr, K. Gméling, and Z. Kasztovszky (2009), Lithium, boron and chlorine as tracers for metasomatism in high-pressure metamorphic rocks: A case study from Syros (Greece), *Mineral. Petrol.*, *95*(3–4), 291–302.
Mason, T. F., D. J. Weiss, M. Horstwood, R. R. Parrish, S. S. Russell, E. Mullane, and B. J. Coles (2004), High-precision Cu and Zn isotope analysis by plasma source mass spectrometry. Part 2. Correcting for mass discrimination effects, *J. Anal. At. Spectrom.*, *19*(2), 218–226.
McDonough, W. F., and S. S. Sun (1995), The composition of the Earth, *Chem. Geol.*, *120*(3), 223–253.
Mevel, C., R. Caby, and J. R. Kienast (1978), Amphibolite facies conditions in the oceanic crust: Example of amphibolitized flaser-gabbro and amphibolites from the Chenaillet ophiolite massif (Hautes Alpes, France), *Earth Planet. Sci. Lett.*, *39*(1), 98–108.
Meyer, J. (1983), The development of the high-pressure metamorphism in the Allalin metagabbro (Switzerland), *Terra Cognita*, *3*(2–3), 187.
Mikutta, C., J. G. Wiederhold, O. A. Cirpka, T. B. Hofstetter, B. Bourdon, and U. Von Gunten (2009), Iron isotope fractionation and atom exchange during sorption of ferrous iron to mineral surfaces, *Geochim. Cosmochim. Acta*, *73*(7), 1795–1812.
Millet, M. A., J. A. Baker, and C. E. Payne (2012), Ultra-precise stable Fe isotope measurements by high resolution multiple-collector inductively coupled plasma mass spectrometry with a ^{57}Fe–^{58}Fe double spike, *Chem. Geol.*, *304*, 18–25.
Moeller, K., R. Schoenberg, R. B. Pedersen, D. Weiss, and S. Dong (2012), Calibration of the new certified reference materials ERM-AE633 and ERM-AE647 for copper and IRMM-3702 for zinc isotope amount ratio determinations, *Geostand. Geoanal. Res.*, *36*(2), 177–199.
Moynier, F., F. Albarède, and G. F. Herzog (2006), Isotopic composition of zinc, copper, and iron in lunar samples, *Geochim. Cosmochim. Acta*, *70*(24), 6103–6117.
Nebel, O., P. Z. Vroon, D. F. Wiggers de Vries, F. E. Jenner, and J. A. Mavrogenes (2010), Tungsten isotopes as tracers of core–mantle interactions: The influence of subducted sediments, *Geochim. Cosmochim. Acta*, *74*(2), 751–762.
Nebel, O., P. A. Sossi, A. Benard, M. Wille, P. Z. Vroon, and R. J. Arculus (2015), Redox-variability and controls in subduction zones from an iron-isotope perspective, *Earth Planet. Sci. Lett.*, *432*, 142–151.
Parkinson, I. J., and R. J. Arculus (1999), The redox state of subduction zones: Insights from arc-peridotites, *Chem. Geol.*, *160*(4), 409–423.
Pearce, J. A. (1982), Trace element characteristics of lavas from destructive plate boundaries, *Andesites*, *8*, 525–548.
Penniston-Dorland, S. C., S. S. Sorensen, R. D. Ash, and S. V. Khadke (2010), Lithium isotopes as a tracer of fluids in a subduction zone mélange: Franciscan Complex, CA, *Earth Planet. Sci. Lett.*, *292*(1), 181–190.
Penniston-Dorland, S. C., G. E. Bebout, P. A. P. von Strandmann, T. Elliott, and S. S. Sorensen (2012), Lithium and its isotopes as tracers of subduction zone fluids and metasomatic processes: Evidence from the Catalina Schist, California, USA, *Geochim. Cosmochim. Acta*, *77*, 530–545.
Plank, T., and C. H. Langmuir (1993), Tracing trace elements from sediment input to volcanic output at subduction zones, *Nature*, *362*(6422), 739–743.
Plank, T., and C. H. Langmuir (1998), The chemical composition of subducting sediment and its consequences for the crust and mantle, *Chem. Geol.*, *145*(3), 325–394.
Pogge von Strandmann, P. A., R. Dohmen, H. R. Marschall, J. C. Schumacher, and T. Elliott (2015), Extreme magnesium isotope fractionation at outcrop scale records the mechanism and rate at which reaction fronts advance. *J. Petrol.*, *56*(1), 33–58.
Polyakov, V. B., and S. D. Mineev (2000), The use of Mössbauer spectroscopy in stable isotope geochemistry, *Geochim. Cosmochim. Acta*, *64*(5), 849–865.
Pons, M. L., G. Quitté, T. Fujii, M. T. Rosing, B. Reynard, F. Moynier, C. Douchet, and F. Albarède (2011), Early Archean serpentine mud volcanoes at Isua, Greenland, as a niche for early life, *Proc. Natl. Acad. Sci. U. S. A.*, *108*(43), 17,639–17,643.
Pons, M. L., B. Debret, P. Bouilhol, A. Delacour, and H. Williams (2016), Zinc isotope evidence for sulfate-rich fluid transfer across subduction zones, *Nat. Commun.*, *7*, 13794.
Rouxel, O., N. Dobbek, J. Ludden, and Y. Fouquet (2003), Iron isotope fractionation during oceanic crust alteration, *Chem. Geol.*, *202*(1), 155–182.
Rouxel, O., W. C. Shanks, W. Bach, and K. J. Edwards (2008), Integrated Fe-and S-isotope study of seafloor hydrothermal vents at East Pacific Rise 910 N, *Chem. Geol.*, *252*(3), 214–227.
Rubatto, D., D. Gebauer, and M. Fanning (1998), Jurassic formation and Eocene subduction of the Zermatt–Saas-Fee ophiolites: Implications for the geodynamic evolution of the Central and Western Alps, *Contrib. Mineral. Petrol.*, *132*(3), 269–287.
Rüpke, L. H., J. P. Morgan, M. Hort, and J. A. Connolly (2004), Serpentine and the subduction zone water cycle, *Earth Planet. Sci. Lett.*, *223*(1), 17–34.
Scambelluri, M., and P. Philippot (2001), Deep fluids in subduction zones, *Lithos*, *55*(1), 213–227.
Scambelluri, M., E. Rampone, and G. B. Piccardo (2001), Fluid and element cycling in subducted serpentinite: A trace-element study of the Erro–Tobbio high-pressure ultramafites (Western alps, NW Italy), *J. Petrol.*, *42*(1), 55–67.
Scambelluri, M., T. Pettke, E. Rampone, M. Godard, and E. Reusser (2014), Petrology and trace element budgets of high-pressure peridotites indicate subduction dehydration of serpentinized mantle (Cima di Gagnone, Central Alps, Switzerland), *J. Petrol.*, *55*(3), 459–498.
Scambelluri, M., and S. Tonarini (2012), Boron isotope evidence for shallow fluid transfer across subduction zones by serpentinized mantle, *Geology*, *40*(10), 907–910.
Schauble, E. A. (2004), Applying stable isotope fractionation theory to new systems, *Rev. Mineral. Geochem.*, *55*, 65–102.
Schmidt, M. W., and S. Poli (2014), Devolatisation during subduction, in *The Crust, Treatise on Geochemistry*, edited by H. D. Holland and K. K. Turekian, pp. 669–701, Elsevier-Pergamon, Oxford, U. K.
Schuessler, J. A., R. Schoenberg, and O. Sigmarsson (2009), Iron and lithium isotope systematics of the Hekla volcano, Iceland—Evidence for Fe isotope fractionation during magma differentiation, *Chem. Geol.*, *258*(1), 78–91.
Schwartz, S., S. Guillot, B. Reynard, R. Lafay, B. Debret, C. Nicollet, P. Lanari, and A. L. Auzende (2013), Pressure–temperature estimates of the lizardite/antigorite transition in high pressure serpentinites, *Lithos*, *178*, 197–210.

Sossi, P. A., G. P. Halverson, O. Nebel, and S. M. Eggins (2015), Combined separation of Cu, Fe and Zn from rock matrices and improved analytical protocols for stable isotope determination, *Geostand. Geoanal. Res.*, *39*(2), 129–149.
Sossi, P. A., O. Nebel, and J. Foden (2016), Iron isotope systematics in planetary reservoirs, *Earth Planet. Sci. Lett.*, *452*, 295–308.
Teng, F.-Z., W. F. McDonough, R. L. Rudnick, and R. J. Walker (2006), Diffusion-driven extreme lithium isotopic fractionation in country rocks of the Tin Mountain pegmatite, *Earth Planet. Sci. Lett.*, *243*(3), 701–710.
Teng, F. Z., N. Dauphas, and R. T. Helz (2008), Iron isotope fractionation during magmatic differentiation in Kilauea Iki lava lake, *Science*, *320*(5883), 1620–1622.
Teng, F. Z., N. Dauphas, R. T. Helz, S. Gao, and S. Huang (2011), Diffusion-driven magnesium and iron isotope fractionation in Hawaiian olivine, *Earth Planet. Sci. Lett.*, *308*(3), 317–324.
Telus, M., N. Dauphas, F. Moynier, F. L. Tissot, F. Z. Teng, P. I. Nabelek, P. R. Craddock, and L. A. Groat (2012), Iron, zinc, magnesium and uranium isotopic fractionation during continental crust differentiation: The tale from migmatites, granitoids, and pegmatites, *Geochim. Cosmochim. Acta*, *97*, 247–265.
Teng, F. Z., N. Dauphas, S. Huang, and B. Marty (2013), Iron isotopic systematics of oceanic basalts, *Geochim. Cosmochim. Acta*, *107*, 12–26.
Testemale, D., J. Brugger, W. Liu, B. Etschmann, and J. L. Hazemann (2009), In-situ X-ray absorption study of iron (II) speciation in brines up to supercritical conditions, *Chem.l Geol.*, *264*(1), 295–310.
Tricart, P. (1984), From passive margin to continental collision; a tectonic scenario for the Western Alps, *Am. J. Sci.*, *284*(2), 97–120.
Tricart, P., and S. Schwartz (2006), A north-south section across the Queyras Schistes lustrés (Piedmont zone, western Alps): Syn-collision refolding of a subduction wedge, *Eclogae Geol. Helv.*, *99*(3), 429–442.
Ulmer, P., and V. Trommsdorff (1995), Serpentine stability to mantle depths and subduction-related magmatism, *Science*, *268*(5212), 858.
Urey, H. C. (1947), The thermodynamic properties of isotopic substances, *J. Chem. Soc.*, *0*, 562–581.
Vils, F., O. Müntener, A. Kalt, and T. Ludwig (2011), Implications of the serpentine phase transition on the behaviour of beryllium and lithium–boron of subducted ultramafic rocks, *Geochim. Cosmochim. Acta*, *75*(5), 1249–1271.
Vitale Brovarone, A., and O. Beyssac (2014), Lawsonite metasomatism: A new route for water to the deep Earth, *Earth Planet. Sci. Lett.*, *393*, 275–284.
Wang, Z.-Z., S.-A. Liu, J. Liu, J. Huang, Y. Xiao, Z.-Y. Chu, X.-M. Zhao, and L. Tang (2017), Zinc isotope fractionation during mantle melting and constraints on the Zn isotope composition of Earth's upper mantle, *Geochim. Cosmochim. Acta*, *198*, 151–167.
Weyer, S., and D. A. Ionov (2007), Partial melting and melt percolation in the mantle: The message from Fe isotopes, *Earth Planet. Sci. Lett.*, *259*(1), 119–133.
Weyer, S., and J. B. Schwieters (2003), High precision Fe isotope measurements with high mass resolution MC-ICPMS, *Int. J. Mass Spectrom.*, *226*(3), 355–368.
Weyer, S., and H. M. Seitz (2012), Coupled lithium-and iron isotope fractionation during magmatic differentiation, *Chem. Geol.*, *294*, 42–50.
Weyer, S., A. D. Anbar, G. P. Brey, C. Münker, K. Mezger, and A. B. Woodland (2005), Iron isotope fractionation during planetary differentiation, *Earth Planet. Sci. Lett.*, *240*(2), 251–264.
Williams, H. M., and M. Bizimis (2014), Iron isotope tracing of mantle heterogeneity within the source regions of oceanic basalts, *Earth Planet. Sci. Lett.*, *404*, 396–407.
Williams, H. M., C. A. McCammon, A. H. Peslier, A. N. Halliday, N. Teutsch, S. Levasseur, and J. P. Burg (2004), Iron isotope fractionation and the oxygen fugacity of the mantle, *Science*, *304*(5677), 1656–1659.
Williams, H. M., A. H. Peslier, C. McCammon, A. N. Halliday, S. Levasseur, N. Teutsch, and J. P. Burg (2005), Systematic iron isotope variations in mantle rocks and minerals: The effects of partial melting and oxygen fugacity, *Earth Planet. Sci. Lett.*, *235*(1), 435–452.
Williams, H. M., S. G. Nielsen, C. Renac, W. L. Griffin, S. Y. O'Reilly, C. A. McCammon, N. Pearson, F. Viljoen, J. C. Alt, and A. N. Halliday (2009), Fractionation of oxygen and iron isotopes by partial melting processes: Implications for the interpretation of stable isotope signatures in mafic rocks, *Earth Planet. Sci. Lett.*, *283*(1), 156–166.
Zack, T., and T. John (2007), An evaluation of reactive fluid flow and trace element mobility in subducting slabs, *Chem. Geol.*, *239*(3), 199–216.